Available online at www.sciencedirect.com
ScienceDirect
Geochimica et Cosmochimica Acta 75 (2011) 2170–2186
Geochimica et Cosmochimica Acta
www.elsevier.com/locate/gca

A lattice Boltzmann model for noble gas diffusion in solids: The importance of domain shape and diffusive anisotropy and implications for thermochronometry

Christian Huber [a], William S. Cassata [b,c,*], Paul R. Renne [b,c]

[a] School of Earth and Atmospheric Science, Georgia Institute of Technology, 311 Ferst Drive, Atlanta, GA 30332, USA
[b] Department of Earth and Planetary Sciences, University of California - Berkeley, 307 McCone Hall #4767, Berkeley, CA 94720-4767, USA
[c] Berkeley Geochronology Center, 2455 Ridge Road, Berkeley, CA 94709, USA

Received 4 August 2010; accepted in revised form 24 January 2011; available online 4 March 2011

Abstract

Thermochronometry based on radiogenic noble gases is critically dependent upon accurate knowledge of the kinetics of diffusion. With few exceptions, complex natural crystals are represented by ideal geometries such as infinite sheets, infinite cylinders, or spheres, and diffusivity is assumed to be isotropic. However, the physical boundaries of crystals generally do not conform to ideal geometries and diffusion within some crystals is known to be anisotropic. Our failure to incorporate such complexities into diffusive models leads to inaccuracies in both thermal histories and diffusion parameters calculated from fractional release data. To address these shortcomings we developed a code based on the lattice Boltzmann (LB) method to model diffusion from complex 3D geometries having isotropic, temperature-independent anisotropic, and temperature-dependent anisotropic diffusivity. In this paper we outline the theoretical basis for the LB code and highlight several advantages of this model relative to more traditional finite difference approaches. The LB code, along with existing analytical solutions for diffusion from simple geometries, is used to investigate the affect of intrinsic crystallographic features (e.g., crystal topology and diffusion anisotropy) on calculated diffusion parameters and a novel method for approximating thermal histories from crystals with complex topologies and diffusive anisotropy is presented.

1. INTRODUCTION

The $^{40}Ar/^{39}Ar$, $^{4}He/^{3}He$, and (U–Th)/He techniques have emerged as powerful tools for quantifying low-temperature thermal histories of rocks. The accuracy of results obtained from these methods is critically dependent on our knowledge of Ar and He diffusion kinetics (E_a and D_o) in the minerals of interest (e.g., K-feldspar, biotite, hornblende, plagioclase, apatite, zircon, titanite, etc.). Published diffusion parameters used in thermochronometry are commonly derived from degassing experiments relating fractional loss to diffusivity (D) based on analytical solutions for simple geometries, such as an infinite cylinder, infinite sheet, sphere, or cube, assuming that diffusion is isotropic. However, the physical boundaries of crystals, which have been shown to define the diffusion domain in many cases (e.g., Goodwin and Renne, 1991; Wright et al., 1991; Wartho et al., 1999; Farley, 2000; Farley and Reiners, 2001), commonly have more complex shapes, which raises the question of how seriously the idealization of geometry affects the accuracy of results. Furthermore, given the structural anisotropy of many minerals, the possibility of diffusion anisotropy must be considered. Only rarely have empirical studies documented anisotropy of noble gas diffusion in crystals (e.g., Giletti, 1974; Hames and Bowring, 1994; Farley, 2000, 2007; Reich et al., 2007; Cherniak et al., 2009; Saadoune and De Leeuw, 2009; Saadoune

* Corresponding author. Tel.: +1 7738028146.
E-mail addresses: christian.huber@eas.gatech.edu (C. Huber), cassata@berkeley.edu (W.S. Cassata), prenne@bgc.org (P.R. Renne).

0016-7037/$ - see front matter © 2011 Elsevier Ltd. All rights reserved.
doi:10.1016/j.gca.2011.01.039

et al., 2009), but it can be argued that few experiments have been employed that would detect such a feature.

In this paper we describe a code based on the lattice Boltzmann (LB) method to model diffusion from complex 3D crystal domains having isotropic, temperature-independent anisotropic, and temperature-dependent anisotropic diffusivity. We use the code to (1) assess the affect of intrinsic crystallographic features (e.g., crystal topology and diffusion anisotropy) on diffusion parameters obtained by regressing D/a^2 values calculated from fractional loss data using analytical solutions for simple geometries like an infinite sheet or a sphere, and (2) validate a novel method for approximating thermal histories from crystals with complex topologies and diffusive anisotropy. The methods and results presented in these papers are applicable to both He and Ar diffusion in which the physical crystal defines the domain boundary, or in principle to cases involving subcrystal domains whose shapes can be described.

2. THE PHYSICS

The diffusive transport of chemical elements in a solid is governed by the general diffusion equation, given by

$$\frac{\partial C}{\partial t} = \frac{\partial}{\partial x}\left(D_x \frac{\partial C}{\partial x}\right) + \frac{\partial}{\partial y}\left(D_y \frac{\partial C}{\partial y}\right) + \frac{\partial}{\partial z}\left(D_z \frac{\partial C}{\partial z}\right), \tag{1}$$

where D_i is the molecular diffusion coefficient in the i-direction and $C(x, y, z)$ is the concentration of the species of interest at the spatial location of interest.[1] Molecular diffusion coefficients depend on the chemical and structural characteristics of the solid host, parameterized here with ψ, the local temperature T, and the pressure of confinement p (although they are less sensitive to the latter). Molecular diffusivity is strongly temperature-dependent and can be described by the following Arrhenius relationship

$$D(T, \psi, p) = D_0(\psi, p) \exp\left(-\frac{E_a}{RT}\right), \tag{2}$$

where $D_0(\psi, p)$ is a reference diffusivity extrapolated from infinite temperature, E_a is the activation energy, and R is the gas constant.

The general form of Eq. (1) cannot be solved analytically. However, when the diffusion coefficient is uniform in all crystallographic directions and the initial concentration distribution is homogeneous, one can solve Eq. (1) for simple geometries involving high degrees of symmetry. Analytical solutions for diffusion from a sphere, an infinite sheet, and an infinite cylinder exist because their geometric symmetries reduce Eq. (1) to a one-dimensional (1D) problem with a similarity solution, where the single similarity variable (η) is given by

$$\eta = \frac{r}{\sqrt{Dt}}. \tag{3}$$

The similarity variable is obtained by balancing the left-hand side and the reduced (single term) right-hand side of the 1D form of Eq. (1). The existence of a similarity solution in 1D allows us to normalize the space–time relationship of the diffusion equation in terms of a Fourier number (Fo), given by

$$Fo = \frac{Dt}{L^2}, \tag{4}$$

where L is the natural diffusive length scale (e.g., the radius of the spherical crystal). The concentration profile in a 1D diffusion problem is self-similar (i.e., identical for every problem with the same Fo). In other words, once distance and time are normalized with L and L^2/D, respectively, 1D diffusion profiles calculated with similar initial and boundary conditions are identical, and Fo fully characterizes the state of the system in the absence of a source term such as production by radioactive decay.

Complex geometries cannot be reduced to 1D, and a single similarity variable that captures the whole physics of the problem no longer exists. Up to three similarity variables are required (one for each spatial dimension), which are given by

$$\eta_x = \frac{x}{\sqrt{D_x t}}, \quad \eta_y = \frac{y}{\sqrt{D_y t}}, \quad \eta_z = \frac{z}{\sqrt{D_z t}}. \tag{5}$$

Scaling Eq. (1) with three independent length scales L_x, L_y, and L_z (representing the natural dimensions of a crystal aligned with the Cartesian coordinate axes), we obtain

$$\frac{\partial C}{\partial t^*} = \frac{D_x \tau}{L_x^2}\frac{\partial^2 C}{\partial (x^*)^2} + \frac{D_y \tau}{L_y^2}\frac{\partial^2 C}{\partial (y^*)^2} + \frac{D_z \tau}{L_z^2}\frac{\partial^2 C}{\partial (z^*)^2}, \tag{6}$$

where x^*, y^*, and z^* represent the spatial coordinates normalized by L_x, L_y, and L_z, respectively, and t^* is the dimensionless time normalized by the characteristic timescale of the process of interest (e.g., L_y^2/D_y using the y-axis as a reference).

The following dimensionless numbers are implicit in Eq. (6):

$$Fo_x = \frac{D_x t}{L_x^2}, \quad Fo_y = \frac{D_y t}{L_y^2}, \quad Fo_z = \frac{D_z t}{L_z^2}. \tag{7}$$

For the case of an infinite slab with normal along the x-direction, Fo_x is the only non-zero Fourier number ($Fo_y = Fo_z = 0$). For a sphere, $Fo_x = Fo_y = Fo_z$ and the problem is one dimensional in spherical coordinates. Finally, for an infinite cylinder aligned with z, $Fo_x = Fo_y$ and $Fo_z = 0$ and the problems reduces to a single spatial dimension in cylindrical coordinates.

The relative importance of any two right-hand terms in Eq. (6) is given by the ratio of the dimensionless Fourier numbers. Assuming no anisotropy of diffusivity, diffusion along the axis corresponding to the smallest dimension of the crystal ($L_i < L_{j\neq i}$) dominates the right-hand side of Eq. (6) and largely controls the rate of loss of the diffusant. In the case where $L_i << L_{j\neq i}$, the problem can be reduced to a single Fourier number Fo_i and an analytical similarity solution. Most natural crystals have complex topologies that cannot be reduced to a single similarity variable, and therefore cannot be modeled using simple 1D finite-difference methods, which prompted us to develop a model based on the lattice Boltzmann (LB) method for diffusion.

[1] Eq. (1) is the general diffusion equation in Cartesian coordinates for electrically neutral atoms, in the absence of a production term and Soret effects.

3. THE LATTICE BOLTZMANN CODE

In LB, the physics is not described by continuum mechanics, but rather by the evolution of a set of particle distribution functions f_i from which the continuum mechanics equation can be retrieved as averages. The LB method is based on statistical mechanics (kinetic theory), where continuum equations (e.g., Navier–Stokes, diffusion, etc.) are represented by the advection and collision of particle distribution functions (PDF's). The domain (crystal) is discretized into a lattice wherein the PDF's move from one node to another and redistribute momentum upon collision (Frisch et al., 1986; Qian et al., 1992; Chopard and Droz, 1998). Movement throughout the lattice is described by a discretized version of Boltzmann's equation with a simplified collision frequency ω (Bhatnagar et al., 1954), given by

$$f_i(x + v_i dt, t + dt) - f_i(x, t) = \omega(f_i^{eq}(x, t) - f_i(x, t)), \quad (8)$$

where $\mathbf{x}$ and $\mathbf{v}_i$ are the position on the lattice and the velocity vector connecting two neighbor nodes, respectively (see Fig. A2). Thus Eq. (8) reflects the probability of finding a particle at position $\mathbf{x}$ and time t with velocity $\mathbf{v}_i$. Diffusivity is incorporated in the discretized Boltzmann's equation through the collision frequency ω according to the following equation:

$$D = c_s^2 dt\left(\frac{1}{\omega} - \frac{1}{2}\right), \quad (9)$$

where $c_s{}^2$ is a constant (the "sound speed" of the lattice) that depends on the connectivity of lattice nodes and is equal to 1/3. In this model lattice nodes are simply connected by orthogonal links, which gives rise to five velocity vectors in 2D (north, south, east, west, and rest; D2Q5) and seven velocity vectors in 3D (north, south, east, west, up, down, and rest; D3Q7).

The equilibrium distribution f_i^{eq} is given by

$$f_i^{eq}(x, t) = w_i\, C(x, t), \quad (10)$$

where w_i are the lattice weights equal to 1/3 (w_0) and 1/6 (w_1, w_2, w_3, w_4) for D2Q5 and 1/4 (w_0) and 1/8 (w_1, w_2, w_3, w_4, w_5, w_6) for D3Q7.

We define the local concentration to be the sum of the probability distributions, given by

$$C = \sum_{i=0}^{Q-1} f_i = \sum_{i=0}^{Q-1} f_i^{eq}. \quad (11)$$

where Q is 5 in 2D and 7 in 3D.

After summing the particle distribution functions at each node, the 3D diffusion equation is obtained through a Chapman-Enskog expansion of Eq. (8) (see Wolf-Gladrow (2000) for a derivation of the diffusion equation from Boltzmann's equation). Thus the redistribution of mass within the lattice is described by the 3D diffusion equation. For more information on the development and implementation of lattice Boltzmann methods the reader is referred to Chopard and Droz (1998), Wolf-Gladrow (2000), and Succi (2002).

To model diffusion from arbitrarily complex topologies using the LB code, we designed a novel algorithm based on the idea of a phase transition to fix the concentration at the domain boundary. During a pure substance phase transition, the temperature at the interface between the two substances is constant. When the latent heat of fusion (enthalpy) is arbitrarily large, the interface remains fixed both spatially and at the phase transition temperature. Because heat and mass diffusion are governed by the same equations, concentration is interchangeable with temperature and we can model a fictitious "phase transition" at constant concentration between the diffusing domain and a hypothetical surrounding phase. The fictitious enthalpy is given by

$$H = c_c C + L + \phi, \quad (12)$$

where c_c is the equivalent of a specific heat, L is the latent heat, and ϕ is the melt fraction. The surrounding medium (e.g., a vacuum) is set at the phase transition concentration, which coincides with the boundary concentration C_b. The diffusive flux out of the crystal is absorbed by the latent heat, which is set such that $L/(c_c\ \Delta C) >> 1$, where ΔC is the difference between the initial concentration in the crystal and C_b. Each point of the computational domain (the crystal and surrounding vacuum) is governed by the same equation (diffusion with a latent heat term), which renders the model irrespective of the geometry of the diffusing crystal. This technique obviates the need to interpolate the local diffusive flux at the boundary tangential and normal to the interface. The infinite enthalpy method is described in greater detail in Huber et al. (2008).

The LB code is particularly apt for natural diffusion processes from complex geometries because difficulties associated with rescaling the mean free path between consecutive collisions in Monte Carlo simulations as particles approach the domain boundary (e.g., Gautheron and Tasson-Got, 2010) are obviated. Furthermore, in LB each node can have unique physical properties, including initial concentration and directionally dependent diffusivity. Thus realistic mineralogical and microstructural features like asymmetrical concentration gradients, exsolution lamellae of differing diffusion kinetics, and diffusive sinks are readily incorporated. Lastly, the LB model can be efficiently coded for parallel computing to simulate 3D diffusion problems at high resolution (e.g., 0.1 micron exsolution lamellae). Pending appropriate funding support for development, we anticipate releasing an easy-to-use software package with an extensive graphical user interface in the near future. In the interim, those interested in using the LB method are encouraged to contact us to obtain the existing codes. Additional information on the code can be found at http://huber.eas.gatech.edu/diffusion.html.

4. PROOF OF ACCURACY AND DEMONSTRATION OF BASIC MODELING CAPABILITIES

To validate the accuracy of our model in 3D, we tested it against the analytical solution for diffusive loss from a sphere (Carslaw and Jaeger, 1959; Crank, 1975; see also McDougall and Harrison, 1999). Fig. 1 illustrates the excellent agreement between the analytical solution and the results we obtain from our lattice-Boltzmann diffusion model using the enthalpy method to enforce $C_b = 0$ at the

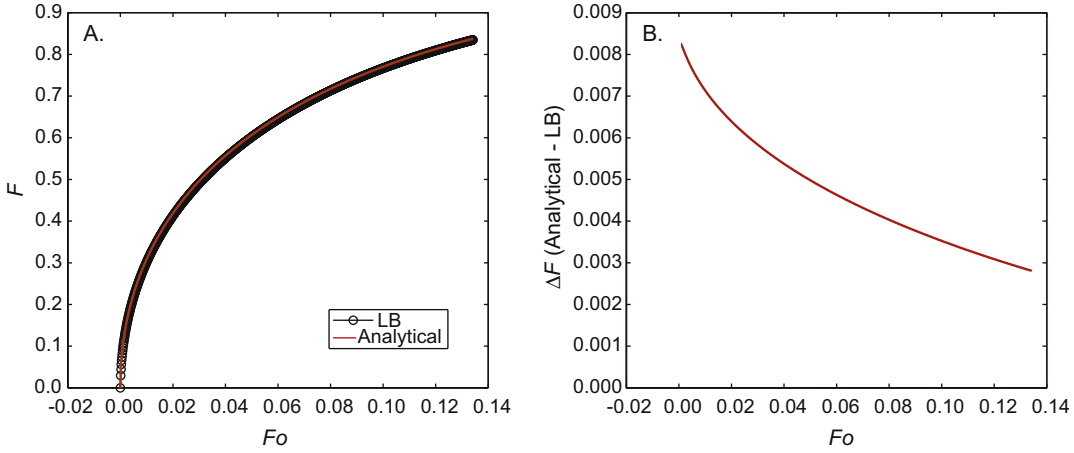

Fig. 1. (A) Plot of fractional loss (F) as a function of Fourier number ($Fo = Dt/a^2$) for the spherical LB model compared to the analytical solution for diffusive loss from a sphere. (B) Difference in fractional loss (analytical solution – LB model) as a function of Fo. The LB code is $> 99\%$ accurate at all Fo.

domain boundary. We used a Cartesian (xyz) grid of 200^3 (8×10^6) nodes for this benchmark calculation. All calculations throughout this paper have a minimum resolution of 50 nodes per crystallographic axis. The numerical model is 2nd order accurate (i.e., accuracy increases with the square of the resolution).

A significant advantage the LB method relative to more traditional finite difference approaches is the ease with which realistic crystal geometries can be modeled. Constructing a crystal in the LB code is much like assembling square blocks into a 3D structure. Complex topologies are discretized into a lattice comprising thousands of nodes. For example, in Fig. 2 we show concentration maps taken from diffusion models of a cube and a tetragonal prism with pyramidal terminations. By inspection of the fractional loss (F) as a function of Fourier number (Fo) shown in Fig. 2, it is clear that the tetragonal prism with pyramidal terminations diffuses at markedly different rate than a similarly sized sphere.

In addition to complex topologies, the LB code is capable of incorporating diffusive anisotropy, either of constant activation energy (E_a) and differing frequency factor (D_o) (temperature-independent anisotropy) or differing E_a and D_o (temperature-dependent anisotropy). Because the diffusive flux in a given crystallographic direction is fully described by the Fourier number ($Fo = Dt/a^2$) for that axis, a doubling of the diffusive lengthscale is mathematically equivalent to reducing the diffusivity by a factor of four. We rely upon this mathematical equivalency of diffusive and geometric anisotropy to validate the accuracy of our model when diffusive anisotropy is incorporated. Fig. 3 depicts F as a function of Fo for several hypothetical rectangular crystals, one of which has temperature-independent anisotropy (same E_a, different D_o). By inspection it is clear that if diffusivity in the longer crystallographic direction is faster by a factor of ε^2, where ε is the aspect ratio, then diffusion proceeds at the same rate as from an $\varepsilon = 1$ rectangle (a perfect square) wherein diffusivity in both directions is isotropic. For example, diffusion from an $\varepsilon = 3$ rectangle with $9\times$ faster diffusivity in the long direction proceeds in the same manner as that from an $\varepsilon = 1$ rectangle wherein diffusivity in both directions is equivalent. We return to

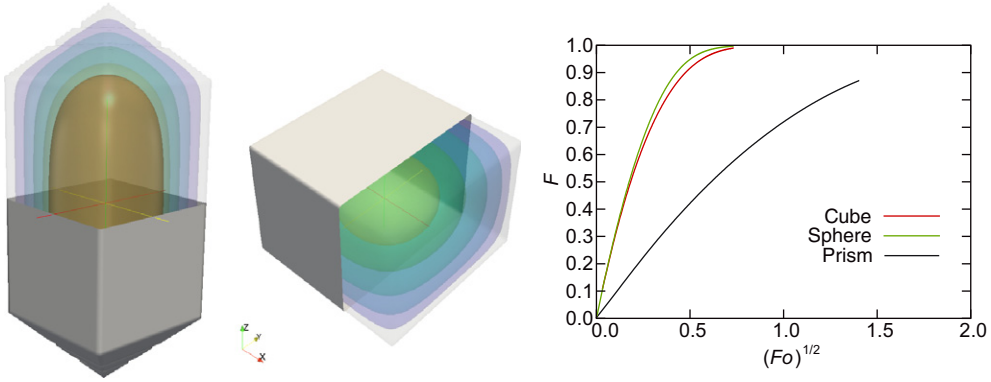

Fig. 2. 3-D diffusion models of a cube (center) and tetragonal prism with pyramidal terminations (left). Color variations represent the 0.3 isoconcentration surface (normalized between 0 and 1) at different time steps. Right: Plot of F vs. $Fo^{1/2}$ ($Fo = Dt/a^2$) for the tetragonal prism with pyramidal terminations, a cube, and a sphere. For each shape "a" in Dt/a^2 is equal to the distance from center of tetragonal prism with pyramidal terminations to the nearest face. (For interpretation of references to color in this figure legend, the reader is referred to the web version of this article.)

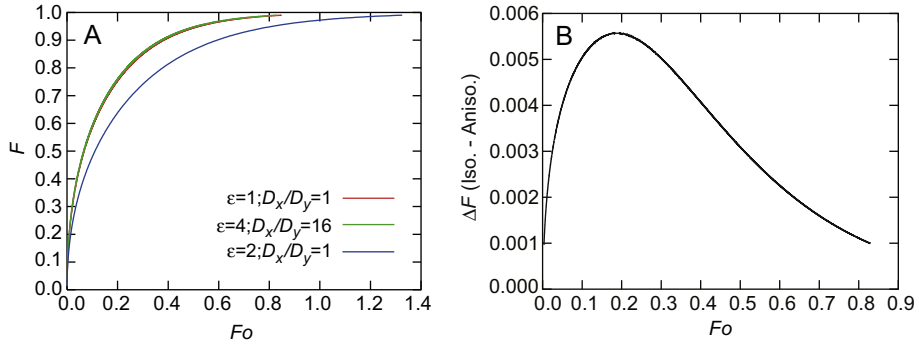

Fig. 3. (A) Comparison of fractional loss (F) as a function of Fourier number (Fo) for three hypothetical rectangular crystals of aspect ratio (ε) between 1 and 4. The $\varepsilon = 4$ rectangle has temperature-independent anisotropy, where diffusivity in longer crystallographic direction is 16× faster than the shorter direction. Because the diffusivity in the longer direction is faster by a factor of ε^2, diffusion proceeds at the same rate as from the $\varepsilon = 1$ rectangle with isotropic diffusivity. (B) Difference in F (isotropic-anisotropic) as a function of Fo. Geometric and diffusive anisotropy are indistinguishable to > 99%, which is within the numerical uncertainty of the LB code at the resolution of these models ($50 \times 50\varepsilon$ nodes).

the concept of the mathematical equivalency of diffusive and geometric anisotropy in the following section.

Temperature-dependent anisotropy (different E_a) can also be incorporated into the LB code. To illustrate this feature we have generated an Arrhenius plot from a hypothetical rectangular crystal wherein diffusion along the shorter crystallographic axis has a lower E_a for diffusion (46.7 kJ/mole) than the longer axis (170 kJ/mole) (Fig. 4). The Arrhenius relationships intersect (define a "kinetic crossover"; Reiners, 2009) at 800 °C. Thus at lower temperatures diffusion proceeds primarily along the short axis and at higher temperatures diffusion proceeds primarily along the long axis. At temperatures in the vicinity of the kinetic crossover, diffusion proceeds along both axes at similar rates. By inspection of Fig. 4 it is evident that crystals having temperature-dependent diffusive anisotropy yield upwardly kinked or curved Arrhenius plots [see also Watson et al. (2010)]. The extent to which an Arrhenius array is curved or kinked depends upon the contrast in E_a and D_o and the aspect ratios of the axes. In the following section we show that crystals having non-ideal geometries and/or temperature-independent anisotropy also yield curved Arrhenius arrays.

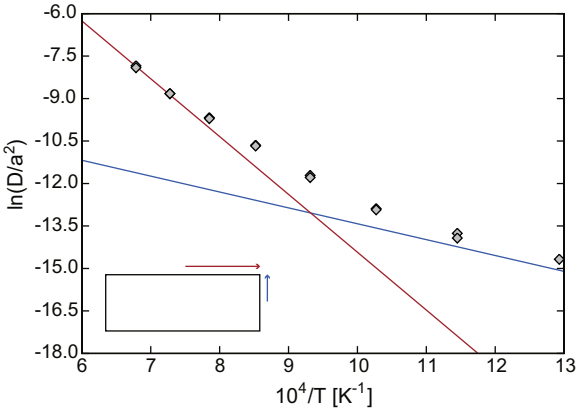

Fig. 4. Arrhenius plot for a hypothetical rectangular crystal having temperature-dependent anisotropy. The red and blue lines are the Arrhenius relationships that define diffusion in the E–W and N–S crystallographic directions, respectively (see inset). The Arrhenius array that results from the incremental degassing of this rectangle (grey diamonds) is curved with a pronounced upward inflection, which reflects the transition from diffusion proceeding predominately along the shorter crystallographic direction at low-T to the longer crystallographic direction at high-T. (For interpretation of the references to color in this figure legend, the reader is referred to the web version of this article.)

5. THE IMPORTANCE OF DOMAIN SHAPE AND DIFFUSIVE ANISOTROPY ON CALCULATED DIFFUSION PARAMETERS

Diffusion parameters (E_a and D_o) are commonly derived from degassing experiments relating fractional loss to diffusivity using analytical solutions for simple geometries, such as an infinite sheet or sphere. However, these two end-member diffusive geometries (i.e., the maximum and minimum surface area to volume ratio for a given diffusive radius, respectively) are not representative of most natural crystals. Assuming that natural crystals can be represented by spheres *a priori* overestimates the diffusive isotropy in 3D, whereas assuming they can be represented by infinite sheets *a priori* underestimates the isotropy in 3D. Plotting a given set of fractional release data on an Arrhenius plot using analytical solutions for both geometries places bounds on the E_a and D_o/a^2 of the crystal, but does not constrain the true diffusion parameters of the sample of interest. Here we use both analytical solutions and the LB model to assess the inherent inaccuracies in diffusion parameters derived in this manner.

In Fig. 5 four sets of fractional release data calculated for the incremental degassing of an infinite sheet (2 sets) and a sphere (2 sets) are plotted on Arrhenius diagrams using analytical solutions for both geometries (complete stepwise degassing data can be found in the Supplementary Files Table 1). Two important conclusions can be drawn from Fig. 5. First, only the Arrhenius arrays

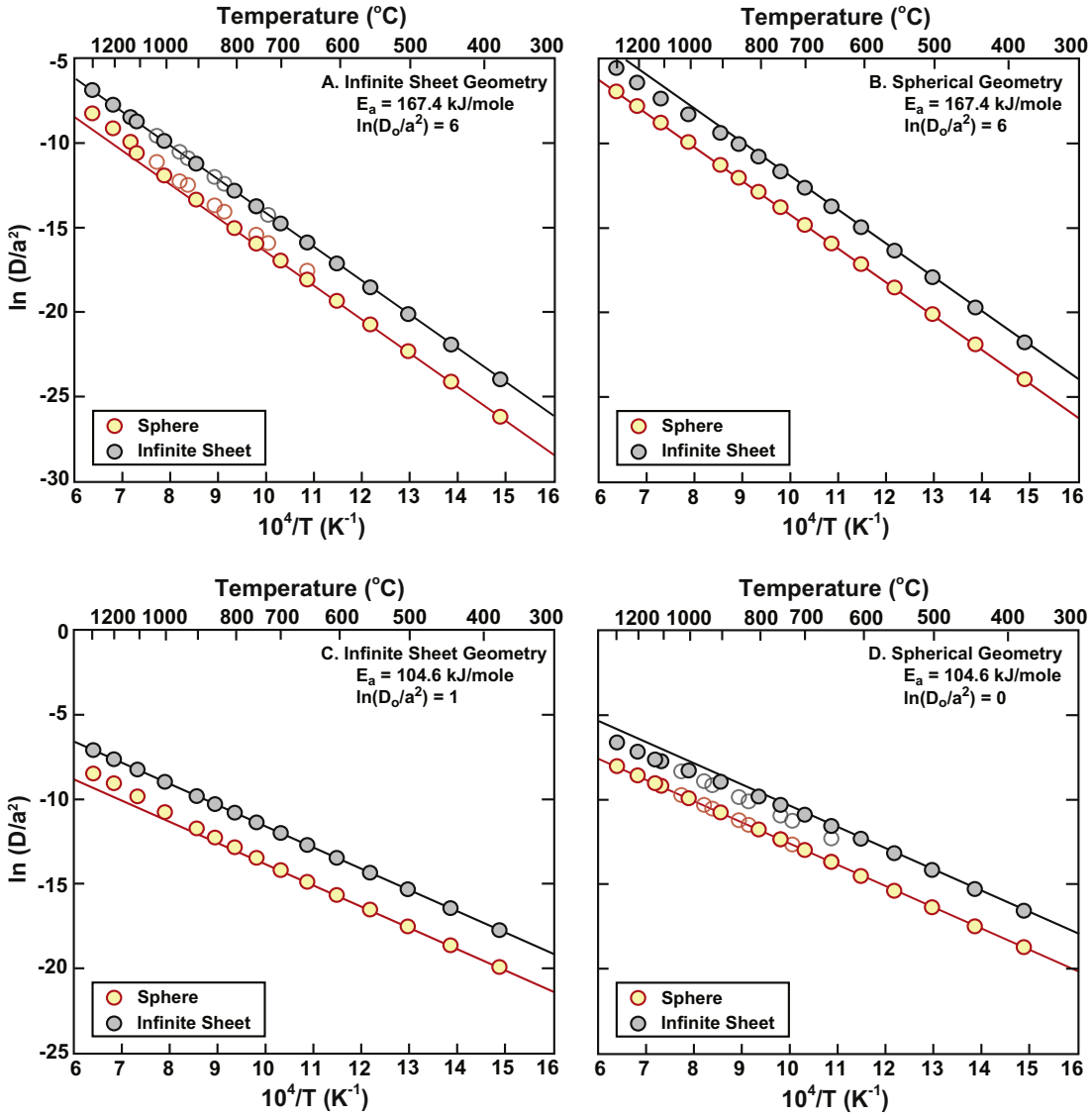

Fig. 5. Arrhenius plots calculated for the fractional release data shown in the Supplementary Files Table 1. Each set of fractional release data is plotted using analytical solutions for spherical and infinite sheet geometries. Fractional release data were obtained from the incremental degassing of (A) an infinite sheet with E_a = 167.4 kJ/mole, (B) a sphere with E_a = 167.4 kJ/mole, (C) an infinite sheet with E_a = 104.6 kJ/mole, (D) a sphere with E_a = 104.6 kJ/mole. Only the Arrhenius arrays plotted using the appropriate geometry are linear.

plotted using the appropriate geometry are linear. The fractional release data for the sphere yield downwardly curved Arrhenius arrays when plotted using analytical solutions for an infinite sheet. The fractional release data for the infinite sheet yield upwardly curved Arrhenius arrays when plotted using analytical solutions for a sphere. The calculated E_a's are relatively accurate at low F and become increasingly erroneous when more gas is included in the regression (Fig. 6). This can be understood by inspecting a plot of F vs. Fo for a sphere and infinite sheet (Fig. 7). At low F both geometries have a similar slope but become increasingly divergent at moderate Fo. The second important conclusion that can be drawn from Fig. 5 is that because the Arrhenius arrays are not parallel (i.e., they define different E_a's), it is not possible to model an infinite sheet as a sphere and vice versa by simply using an effective spherical equivalent radius. If it were possible, the data would have the same E_a, but D_o/a^2 would differ by the square of the spherical equivalent radius.

To assess the magnitude of the error in E_a as a function of crystal geometry and roundness, we used the LB code to simulate diffusion from suites of 2D ovoidal and rectangular crystals with aspect ratios ($\varepsilon = a/b$) ranging from 1 to 10. The shorter dimension ($2b$) was fixed at 100 microns. Thus the shortest distance from the center of each crystal to the nearest edge (b) was 50 microns. We subjected each hypothetical crystal to a typical $^{40}Ar/^{39}Ar$ heating schedule (600 s at 500, 600, 700, …, 1200 °C). Diffusion was governed by the following Arrhenius relationship:

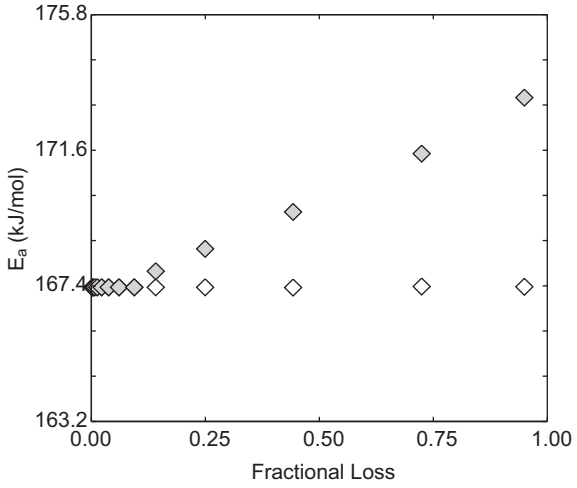

Fig. 6. Plot of activation energy (E_a) as a function of the fraction of gas included in the Arrhenius regression (F) for spherical and infinite sheet geometries. The fractional release data were obtained from the incremental degassing of an infinite sheet with $E_a = 167.4$ kJ/mole. The Arrhenius array calculated using analytical solutions for a sphere (the wrong geometry) becomes increasingly erroneous and curvilinear when more gas fractions are included in the regression.

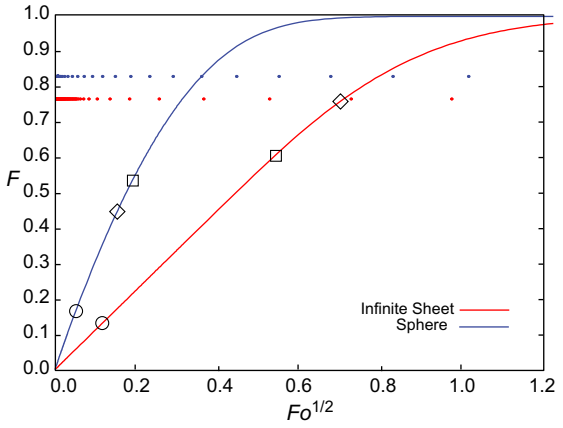

Fig. 7. Plot of fractional loss (F) as a function of the square root of the Fourier number ($Fo = Dt/a^2$) for an infinite sheet and a sphere. The symbols represent the fractional loss that is calculated for heating an $\varepsilon = 1$ rectangle for 600 s at 900 °C (circles), 600 s at 1100 °C (squares), and 1000 years at 350 °C (diamonds) using infinite sheet and spherical geometries. The apparent Fo's obtained assuming infinite sheet and spherical geometries are not identical because geometry-specific E_a and $\ln(D_o/a^2)$ values calculated from the incremental degassing of the $\varepsilon = 1$ rectangle were used (i.e., D at 900 °C is different for spherical and infinite sheet geometries; diffusion parameters are listed in Table 1). Depending on the nature of the heating event, infinite sheet and spherical geometries predict substantially different F. Small dots (blue – sphere; red – infinite sheet) represent the cumulative Fo's experienced by 100 discrete production steps (evenly spaced) from the thermal history shown in Fig. 12a and b. Early productions steps experience larger cumulative Fo whereas later production steps experience smaller cumulative Fo. (For interpretation of the references to color in this figure legend, the reader is referred to the web version of this article.)

$$\ln(D) = \ln(D_o) - \left(\frac{E_a}{RT}\right) = \left(\frac{-13.8\ \mathrm{m}^2}{s}\right) - \left(\frac{170\ \mathrm{kJ/mole}}{RT}\right). \tag{13}$$

To compare the true Arrhenius relationship to those calculated from the step-heating data, we normalized Eq. (13) to the diffusive lengthscale (r) by setting $r = b = 50$ microns, which yields

$$\ln\left(\frac{D}{r^2}\right) = \left(\frac{6}{s}\right) - \left(\frac{170\ \mathrm{kJ/mole}}{RT}\right). \tag{14}$$

We calculated apparent diffusion parameters for each hypothetical crystal using equations for both infinite sheet and spherical geometries. The results are summarized in Fig. 8 and Table 1. All E_a and $\ln(D_o/a^2)$ regressions included >95% of the total gas released, and therefore represent the maximum error in Ea for a given aspect ratio. Conversely, $\ln(D_o/a^2)$ tends to become increasingly accurate when more gas is included in the regression. Thus E_a's are relatively accurate at low F (Fig. 6) whereas $\ln(D_o/a^2)$ values are inaccurate and vice versa.

In Fig. 8A and B we show apparent E_a and $\ln(D_o/a^2)$ values calculated for the ovoidal and rectangular shapes assuming infinite sheet geometry. By inspection it is evident that as crystals deviate from ideal infinite sheet geometry ($\varepsilon = \infty$), the E_a's determined using fractional release data increasingly underestimate the true E_a (170 kJ/mol), attaining a maximum error of ~5% for perfect squares and circles ($\varepsilon = 1$; i.e., an infinite cylinder). There is a noticeable offset between $\ln(D_o/a^2)$ values obtained from the ovoidal and rectangular suites at a given ε value, where the ovoidal shape is characterized by the larger of the two values. This disparity reflects the fact that at a given temperature the proportion of total gas lost from rectangular shapes is inhibited relative to ovoidal shapes of equivalent aspect ratios because the average radial distance to the edge is greater. However, because the relative quantities of gas lost in successive extractions appear to be quite similar, both geometric suites yield equivalent E_a's at a given aspect ratio.

In Fig. 8C and D we show apparent E_a and $\ln(D_o/a^2)$ values calculated for the ovoidal and rectangular shapes assuming spherical geometry. By inspection it is evident that as crystals deviate from ideal spherical geometry ($\varepsilon = 1$ in 3D), the E_a's determined using fractional release data increasingly overestimate the true E_a (170 kJ/mol), attaining a maximum error of ~6% for shapes with large aspect ratios ($\varepsilon > 10$; i.e., a infinite sheet). At true E_a's of 80, 120, 150, 200, and 250 kJ/mol, we observe maximum errors in E_a of 8%, 10%, 9%, 8%, and 2%, respectively, for the heating schedules used. Results vary by several percent for different heating schedules. For example, cycled heating drastically reduces the apparent error in E_a (see Fig. 5). The largest disparity in calculated E_a (~10%) represents a reasonable upper bound on the uncertainty that arises from an inappropriate choice of geometry.

To summarize, diffusion parameters obtained from Arrhenius plots calculated using analytical solutions for simple geometries may be subtly but significantly incorrect. All natural crystals should yield modestly curvilinear

Table 1
Summary of diffusion parameters calculated for spherical and infinite sheet geometires.

Shape	ε	Infinite sheet		Sphere	
		E_a (kJ/mol) $\pm 1\sigma$	$\ln(D_o/r^2) \pm 1\sigma$	E_a (kJ/mol) $\pm 1\sigma$	$\ln(D_o/r^2) \pm 1\sigma$
Rectangles	1	160.5 ± 3.0	6.1 ± 0.2	173.0 ± 2.0	5.5 ± 0.2
	2	163.2 ± 3.0	5.8 ± 0.2	174.5 ± 1.0	5.2 ± 0.2
	5	165.0 ± 3.0	5.7 ± 0.2	176.0 ± 2.0	4.9 ± 0.2
	7	167.0 ± 3.0	5.8 ± 0.2	177.5 ± 2.0	5.0 ± 0.2
	10	167.0 ± 3.0	6.1 ± 0.1	178.0 ± 2.0	5.0 ± 0.1
Ovoids	1	162.0 ± 3.0	6.3 ± 0.2	174.0 ± 1.0	5.8 ± 0.2
	2	163.5 ± 3.0	6.0 ± 0.2	174.5 ± 1.0	5.3 ± 0.2
	5	166.0 ± 3.0	6.0 ± 0.2	177.0 ± 1.0	5.3 ± 0.2
	7	166.0 ± 3.0	6.0 ± 0.1	177.0 ± 1.0	5.3 ± 0.1
	10	167.0 ± 3.0	6.0 ± 0.2	178.5 ± 1.0	5.4 ± 0.2

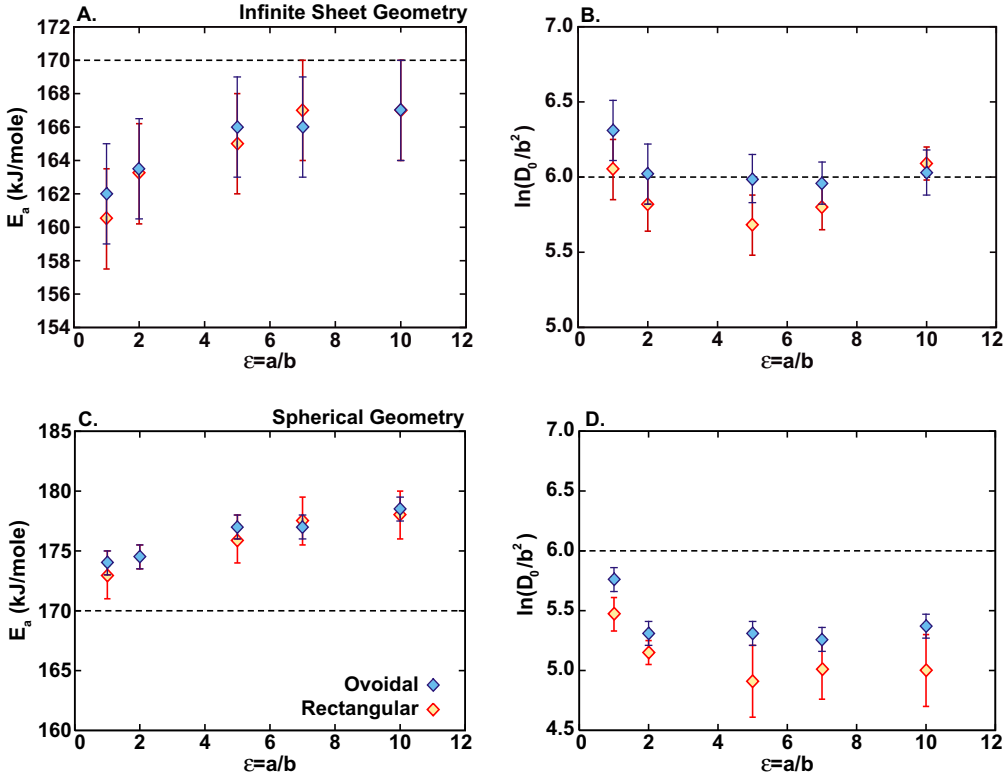

Fig. 8. Apparent diffusion parameters calculated for hypothetical rectangular (red) and ovoidal (blue) crystals with aspect ratios (ε) ranging from 1 to 10. The fractional loss data was generated using the lattice-Boltzmann diffusion model. Diffusion was governed by the Arrhenius relationship presented in Eq. (13) and the true E_a and $\ln(D_o/a^2)$ are shown as dashed lines. Errors are calculated by a least square fit with an Arrhenius relationship of the form $D_0 \exp(-E_a/RT)$. (For interpretation of the references to color in this figure legend, the reader is referred to the web version of this article.)

Arrhenius arrays, where the magnitude of the effect depends on (1) the deviation from an ideal geometry, (2) fractional release included in the regression, and (3) the heating schedule. Regressing a given set of fractional release data using analytical solutions for an infinite sheet and a sphere constrains the minimum and maximum E_a, respectively. A reasonable bound on the maximum intrinsic error in calculated E_a that results from an inappropriate choice of diffusion geometry (or failure to identify to temperature-independent anisotropy, as these are mathematically equivalent) is $\sim$10% for typical Ar and He E_a's. These uncertainties may be significant for modeling thermal histories and comparing diffusion parameters with those obtained from other methods.

6. OBTAINING ACCURATE THERMAL HISTORIES FROM CRYSTALS HAVING GEOMETRIC AND/OR DIFFUSIVE ANISOTROPY

6.1. The AND approach

In Section 5 we discussed the inherent uncertainty on diffusion parameters calculated from fractional release data following Fechtig and Kalbitzer (1966). These uncertainties have been greatly reduced for select minerals that have been characterized using a variety of methods and controlled crystal geometries (e.g., Durango apatite; Farley, 2000). However, even with knowledge of the kinetics that govern diffusion, accurate thermal histories cannot be modeled for crystals with complex geometries using analytical solutions for simple geometries unless corrections are applied to account for deviations from the ideal. These corrections have typically taken the form of an effective, or spherical equivalent, diffusion radius (r_{eff}). Meesters and Dunai (2002) qualitatively addressed this problem with their eigenvalue model, and found that an accurate thermal history could be obtained from a non-spherical crystal if it was modeled as a sphere with an equivalent surface area to volume ratio (hereafter referred to as the SV approach). Watson et al. (2010) addressed a specific form of non-spherical geometry and derived an analytical solution to model diffusion from finite cylinders having anisotropic diffusivity. Gautheron and Tasson-Got (2010) developed a more general approach to modeling complex crystals as spheres based on the concept of the surface area weighted by the relative magnitude of the diffusion coefficients normal to the surface (the active radius model; hereafter referred to as the AR approach). In the following section we discuss the advantages and limitations of the SV and AR approaches and present a new method [Average Normalized Distance (hereafter referred to as the AND approach)] that offers greater accuracy over a wider range of shape and/or diffusive anisotropy.

The physical basis for the SV approach (Meesters and Dunai, 2002) can be understood with a simple mass balance argument, in which the fractional loss is related to the flux out of the surface bounding the diffusing object, given by

$$dF = -\frac{1}{M_0}\oint_S D\frac{\partial C}{\partial n}dS \tag{15}$$

where S is the surface bounding the object, n is the direction of the outward normal to S, and M_0 is the initial concentration integrated over the volume of the object.

If we assume that the diffusive flux out of the surface is homogeneous at any given time, then during an infinitesimal time interval the loss becomes

$$dF \sim \lambda\frac{S}{V}, \tag{16}$$

where λ is a proportionality constant. However, the assumption that the diffusive flux out of any unit surface dS is equivalent is not valid for objects with large shape anisotropy (x/y or $x/z \leqslant 0.1$; Gautheron and Tasson-Got, 2010) and/or diffusion coefficient anisotropy (D_x/D_y or $D_x/D_z \leqslant 0.01$). For example, consider a hypothetical tetragonal prism of dimensions $2x \times 2y \times 2z = 2mm \times 2mm \times 4mm$. Regardless of D_x, D_y, and D_z, the surface area to volume ratio of the isotropic equivalent sphere calculated using the SV approach is 2.5. If $D_x = D_y = 0.5\ D_z$, then the SV approach approximates diffusive loss poorly because of the anisotropic diffusivity in the z direction.

Recently, Gautheron and Tasson-Got (2010) proposed a more general model (the AR approach) to compute a spherical equivalent radius that implicitly incorporates diffusive anisotropy. Unlike the SV approach, which considers only by the physical crystal boundaries, the AR approach effectively rescales the crystal dimensions relative to a reference diffusivity D_a (the average diffusivity in their model). This method relies upon the mathematical equivalency of geometric and diffusive anisotropy discussed in Section 4. Recall that a tetragonal prism of dimensions $2mm \times 2mm \times 4mm$ and diffusivity $D_x = D_y = 0.25\ D_z$ is mathematically equivalent to a tetragonal prism of dimensions $2mm \times 2mm \times 2mm$ and diffusivity $D_x^* = D_y^* = D_z^* = D_x$. The AR approach effectively finds the radius of a sphere with the same surface area to volume ratio as the mathematically equivalent isotropic crystal described above. Thus the integrand in Eq. (16) can more generally be replaced by

$$(\underline{\underline{D}} \bullet \underline{\nabla C}) \bullet \underline{dS}, \tag{17}$$

where a single underline refers to a vector and double underlines to a second rank tensor (matrix). The tensor of diffusivities D can be projected along the normal to the surface element dS to obtain D'

$$\underline{\underline{D'}}\, dS^2 = \underline{dS^T}\ \underline{\underline{D}}\ \underline{dS}, \tag{18}$$

where the superscript T refers to the transpose and dS^2 is the square of the surface area dS. Gautheron and Tassan-Got normalized the diffusivity tensor D' with the average diffusivity D_a to define the active surface element dS', given by

$$\underline{\underline{(D'/D_a)}}\, dS^2 = dS'^2. \tag{19}$$

In the notation of the AR model, the fractional loss out of the diffusing body is given by

$$dF(t) \sim -\frac{1}{M_0}\oint_S D_a \nabla_n C(\underline{x}_s, t) dS'. \tag{20}$$

The equivalent radius for a sphere is such that the loss out of the sphere (dF_{sp}) approximates dF at all time. If we assume that the concentration gradients are homogeneous over the domain boundary, then

$$dF(t) \sim -\frac{D_a}{V C_0}\nabla_s C(t) S'. \tag{21}$$

Similarly the loss out of the equivalent sphere with isotropic diffusivity D_a is

$$dF_{sp}(t) \sim -\frac{D_a}{V_{sp} C_0}\nabla C_{sp}(t) S_{sp}, \tag{22}$$

where the subscript sp was used for the sphere. The active radius is then obtained by matching the losses dF and dF_{sp}, which yields $R_{sp} = 3V/S'$. For isotropic diffusion, the active surface reduces to the physical surface of the diffusing domain and the SV and AR methods are equivalent.

The AR approach is most accurate (F within 5–10% at a given Fo) when the average concentration gradient near the surface matches that of the equivalent sphere (i.e., when the distribution of the diffusing element with respect to the domain boundary is equivalent for the modeled sphere and the actual physical domain). This condition is satisfied within crystals having moderate geometric and/or diffusive anisotropy, which can collectively be parameterized by the following dimensionless numbers:

$$\Omega_1 = \frac{y^2}{x^2}\frac{D_x}{D_y} \tag{23}$$

$$\Omega_2 = \frac{y^2}{z^2}\frac{D_z}{D_y} \tag{24}$$

At Ω_1 and Ω_2 values greater than ~0.01, the AR approach becomes increasingly inaccurate (Gautheron and Tasson-Got, 2010).

We developed a method to calculate a spherical-equivalent correction that is based on the average normalized distance (AND) for diffusion. It is highly accurate (within ~1%) at Ω_1 and Ω_2 values $>10^{-2}$ and better than 5% accurate at Ω_1 and Ω_2 values as low as 10^{-5}. The method can be understood using the moment of inertia of an object as an analogy. An object's moment of inertia describes how it's mass is spatially distributed. Natural crystals and spheres diffusive similarly when the distribution of concentration with respect to the object's boundaries are approximately equivalent at all times. Defining the moment of inertia for diffusion as

$$I_c = \int_V C_0 d(r)^2 dV, \tag{25}$$

where $d(r)$ is the diffusivity-normalized distance to the nearest surface, given by

$$d(r) = \min_i \left(\frac{|\underline{x} - \underline{x}_s|_i}{(D_i/D_{ref})^{1/2}} \right), \tag{26}$$

where i is an index that runs over the Cartesian coordinates (x, y, z) and x and x_s refer to positions inside the domain and on its surface, respectively. D_{ref} is an arbitrary reference diffusivity to which distance is normalized (e.g., the diffusivity in the slowest crystallographic direction). One's choice of D_{ref} does not matter, but it affects the calculated radius of the isotropic equivalent sphere.[2] Thus $d(r)$ is not truly a distance, but rather the fastest way out of the domain, or the direction with the greatest Fourier number (see Fig. 9). In this respect we are again relying on the mathematical equivalency of diffusive and geometric anisotropy. The average normalized distance (AND) for diffusion is therefore given by

$$\mathrm{AND} = \frac{1}{V}\int_V C_0\, d(r)\, dV. \tag{27}$$

[2] In Eqs. (23) and (24), D_y is the reference diffusivity used to calculate Ω_1 and Ω_2. One would calculate a different spherical equivalent radius using the AR approach if diffusivity was cast in terms of D_z.

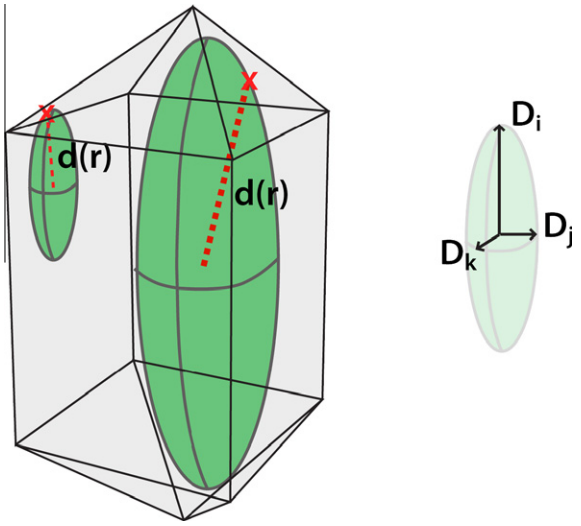

Fig. 9. Schematic illustration of the calculation of the normalized distance $d(r)$ in a tetragonal prism with pyramidal terminations. The semi-axes of the ellipsoid centered at each point $\boldsymbol{x}$ in the crystal are proportional to the tensor of diffusivity. The largest ellipsoid centered on $\boldsymbol{x}$ that remains fully included into the crystal boundaries provides a measure of $d(r)$ at this point. The volumetric average of $d(r)$ yields the AND.

For a sphere with a homogeneous initial concentration distribution and isotropic diffusion, AND is 0.2594 times the radius. Thus mass is distributed in a sphere such that the average displacement of a particle exiting the domain surface is ~26% of the radius. The average, diffusivity-normalized displacement of particles exiting any given geometry can be related to a sphere with the similar moment of inertia for diffusion, the effective radius r_{eff} of which is simply

$$r_{\mathrm{eff}} = \mathrm{AND}/0.2594 \tag{28}$$

For crystals having temperature-independent anisotropy, the ratio of D_{ref} to $D_{x,y,z}$ is fixed, and AND remains constant at all T. For crystals having temperature-dependent anisotropy, AND will vary with temperature according to variations in the diffusivity tensor. AND must be calculated as a function of temperature for samples of this nature and can then be incorporated into finite-difference methods as a temperature-dependent correction to the reference Arrhenius relationship ($D_{ref}(T)$). Because the normalized distance $d(r)$ is independent of the concentration distribution (i.e., it is the normalized distance irrespective of initial location), zoned crystals can also be modeled with AND. That being said, certain complexities intrinsic to zoned samples (e.g., inward and outward diffusion toward areas of lower concentration) cannot be reproduced using an isotropic equivalent sphere with a uniform concentration distribution.

Here we compare results obtained from the AR and AND approaches to illustrate the fidelity of our method. In the following comparisons, we have excluded the SV approach, which is at best as accurate as the AR approach (in the case of isotropic diffusion). Fig. 10 is a plot of F vs. Fo

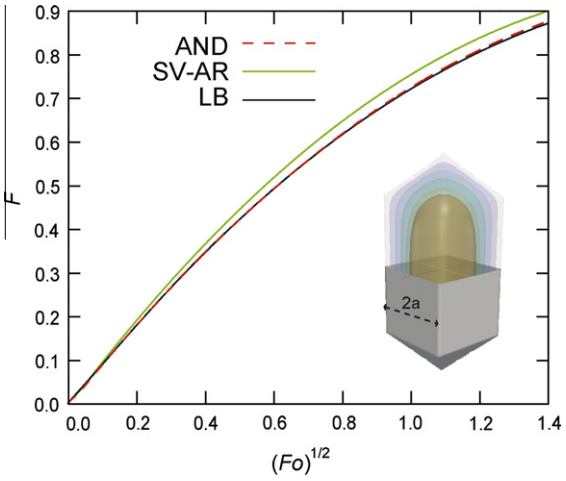

Fig. 10. Plot of F vs. Fo for a tetragonal prism with pyramidal terminations and isotropic equivalent spheres determined using the AND and AR approaches. The relative dimensions of the tetragonal prism are $4 \times 4 \times 7$. The relative height of the pyramidal terminations is 2. Diffusion is isotropic. The AR and AND approaches are accurate to better than 3% and 0.5% at all Fo, respectively.

for a tetragonal prism with pyramidal terminations[3] and the isotropic equivalent spheres determined using the AND and AR approaches. In this example diffusivity in the tetragonal prism with pyramidal terminations is isotropic. The AR approach is accurate to better than 3% at all Fo, while the AND approach is accurate to better than 0.5% at all Fo. The accuracy of the AND approach is more apparent for crystals having greater diffusive or geometric anisotropy. Fig. 11 illustrates the error in fractional loss (ΔF) that results from using the AND and AR approaches to model tetragonal prisms with a range of Ω_1 and Ω_2 values. To construct this figure, F was calculated for the AR and AND approaches at Fo's corresponding to true F of 0.5, 0.7, and 0.9, as constrained by the analytical solution for diffusive loss from a tetragonal prism (see Appendix). By inspections of Fig. 11 it is evident that both the AR and AND methods are accurate to within 5% at $F \leqslant 0.70$. At higher F, the AR approach is inaccurate by as much as 15%. The AND approach is accurate to within ~5% at all F for Ω_1 and Ω_2 values between 10^{-5} and 1.

6.2. Software to calculate AND

AND can be calculated analytically for simple geometries such as tetragonal prisms of dimensions $2x \times 2y \times 2z$ and diffusivity D_x, D_y, D_z (see Appendix). For more complex geometries, we developed a numerical model that runs on any platform (e.g., Windows, Mac, Unix) with a C++ compiler. In this program, the 3D shape is generated from a 3D matrix written in ASCII format, where the scalar value is set to 1 inside the domain and 0 outside. The model computes the normalized radius $x_i/(D_i/D_{ref})^{1/2}$ of the largest ellipsoid centered on each point inside the diffusing domain that remains fully contained within the boundaries of the domain (see Fig. 9). AND is calculated as the volume average of these normalized radii. This code is available for download from http://huber.eas.gatech.edu/diffusion.html. The website includes tutorials for generating matrices in ASCII format using MATLAB.

[3] The tetragonal prism with pyramidal terminations is shown in Fig. 2. The relative dimensions of the tetragonal prism are $4 \times 4 \times 7$. The relative height of the pyramidal terminations is 2.

7. USING SAMPLE SPECIFIC DIFFUSION PARAMETERS

In $^{40}Ar/^{39}Ar$ and $^{4}He/^{3}He$ thermochronometry it is common to determine diffusion kinetics for each sample used for thermal modeling. Lovera et al. (1991) and Meesters and Dunai (2002) noted that one's choice of diffusion geometry negligibly affects modeled thermal histories provided that the same geometry is used to calculate diffusion parameters and forward model potential t–T paths. We conducted a number of modeling exercises to evaluate this hypothesis, and found it to be true for samples that experienced monotonic cooling histories, but not for those subjected to episodic loss events.

7.1. Monotonic cooling histories

To compare modeled thermal histories calculated using infinite sheet and spherical geometries, we generated two "target age spectra" by subjecting a hypothetical infinite sheet to cooling paths that traverse the argon partial retention zone (ArPRZ) over 10 and 100 Ma. We used a finite difference method to model changes in $^{40}Ar^{*}$ concentration through each t–T history, where the mass diffusion equation with a production term was solved implicitly using a Crank–Nicholson scheme. The boundary conditions were zero concentration at the grain edge ($C = 0$ @ $r = R$) and zero flux at the center node ($dC/dr = 0$ @ $r = 0$). After solving for the $^{40}Ar^{*}$ concentration gradient, a uniform ^{39}Ar concentration was imparted to simulate ^{39}Ar production (i.e., by neutron irradiation of K) prior to laboratory analysis. The $^{40}Ar^{*}$ and ^{39}Ar concentration profiles were then degassed incrementally to yield the target age spectra. We calculated diffusion parameters for infinite sheet and spherical geometries from the incremental release of ^{39}Ar. In the case of the infinite sheet, we recover the input diffusion parameters as that geometry was used to generate the target age spectrum ($E_a = 169.5$ kJ/mole, $\ln(D_o/a^2) = 5.92$). In the case of the sphere we obtain erroneous diffusion parameters reflecting our inappropriate choice of diffusion geometry ($E_a = 178.6$ kJ/mole, $\ln(D_o/a^2)$=4.93). We then forward modeled 1000 monotonic cooling histories for both geometries using the geometry-specific diffusion parameters. The resulting model age spectra were compared to the target age spectra and a fit statistic [the mean square of weighted deviates (MSWD; McIntyre et al., 1966)] was calculated for each. Those t–T paths that yielded age spectra that best fit the target spectrum are shown in red in Fig. 12 (MSWD < 3).

By inspection of Fig. 12 it is apparent that both infinite sheet and spherical diffusion geometries predict similar

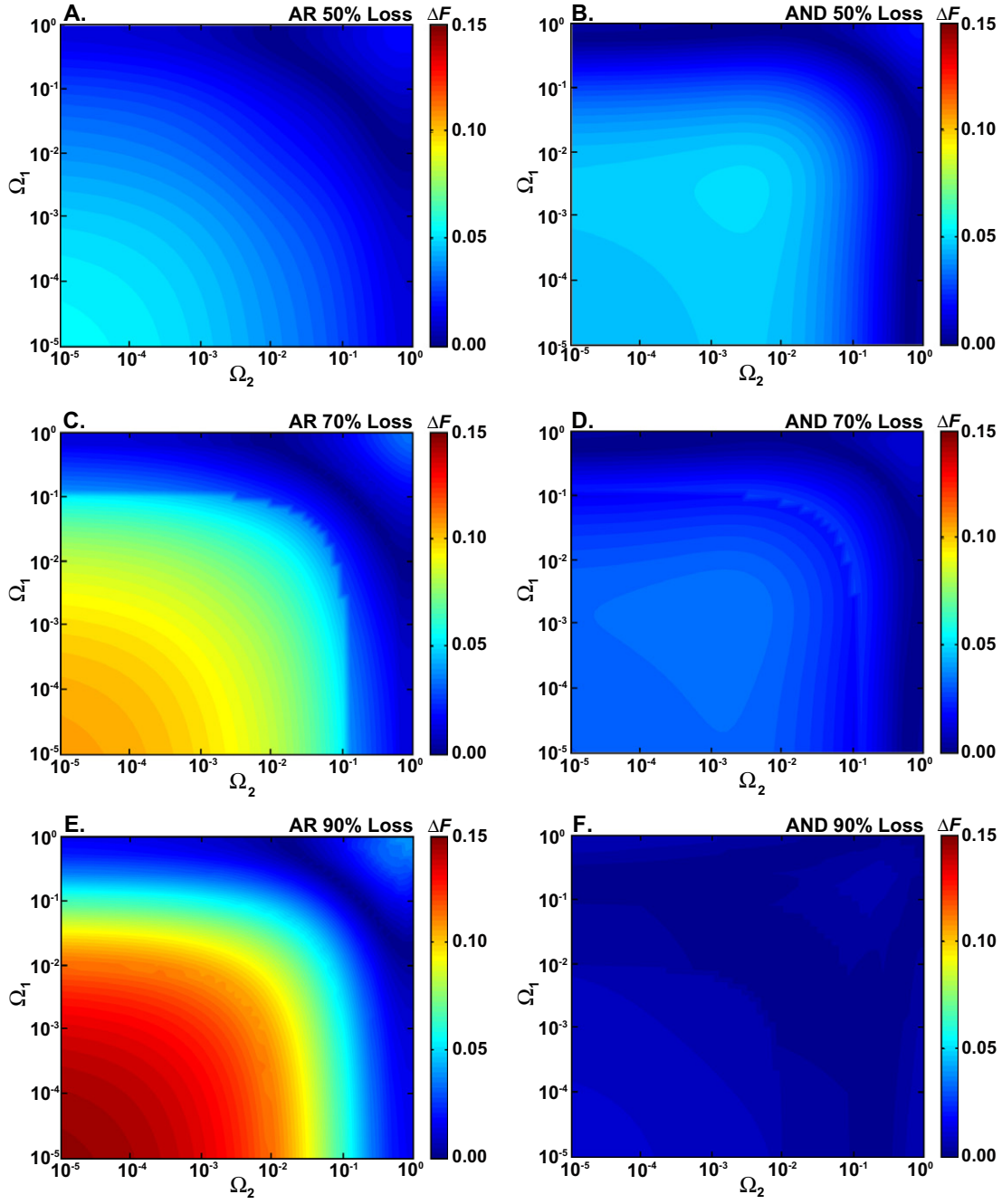

Fig. 11. Comparison of the error in fractional loss (ΔF) at true F of 0.5 (A and B), 0.7 (C and D), and 0.9 (E and F) that results from using the AND and AR approaches to model tetragonal prisms with a range of Ω_1 and Ω_2 values (see text for calculation).

cooling histories for a given target age spectrum. For example, in Fig. 12A and B we show that both geometries predict t–T paths that traverse the ArPRZ from 250 to 200 °C over a 4 Ma interval ending 3 Ma ago. These models support previous assertions [e.g., Lovera et al. (1991) and Meesters and Dunai (2002)] that one's choice of diffusion geometry in a $^{40}Ar/^{39}Ar$ or $^{4}He/^{3}He$ experiment will negligibly influence a calculated thermal history for samples that have cooled monotonically through the PRZ. A logical explanation for this observation is given in Section 7.3.

7.2. Episodic loss events

Extraterrestrial materials (e.g., meteorites and lunar rocks) commonly yield discordant $^{40}Ar/^{39}Ar$ age spectra due to episodic ^{40}Ar loss associated with impact events. To assess the potential error in calculated t–T conditions associated with a given fractional loss (F) that would result from an inappropriate choice of geometry, we modeled a hypothetical infinite tetragonal prism as both an infinite sheet and a sphere and compared the results. For the

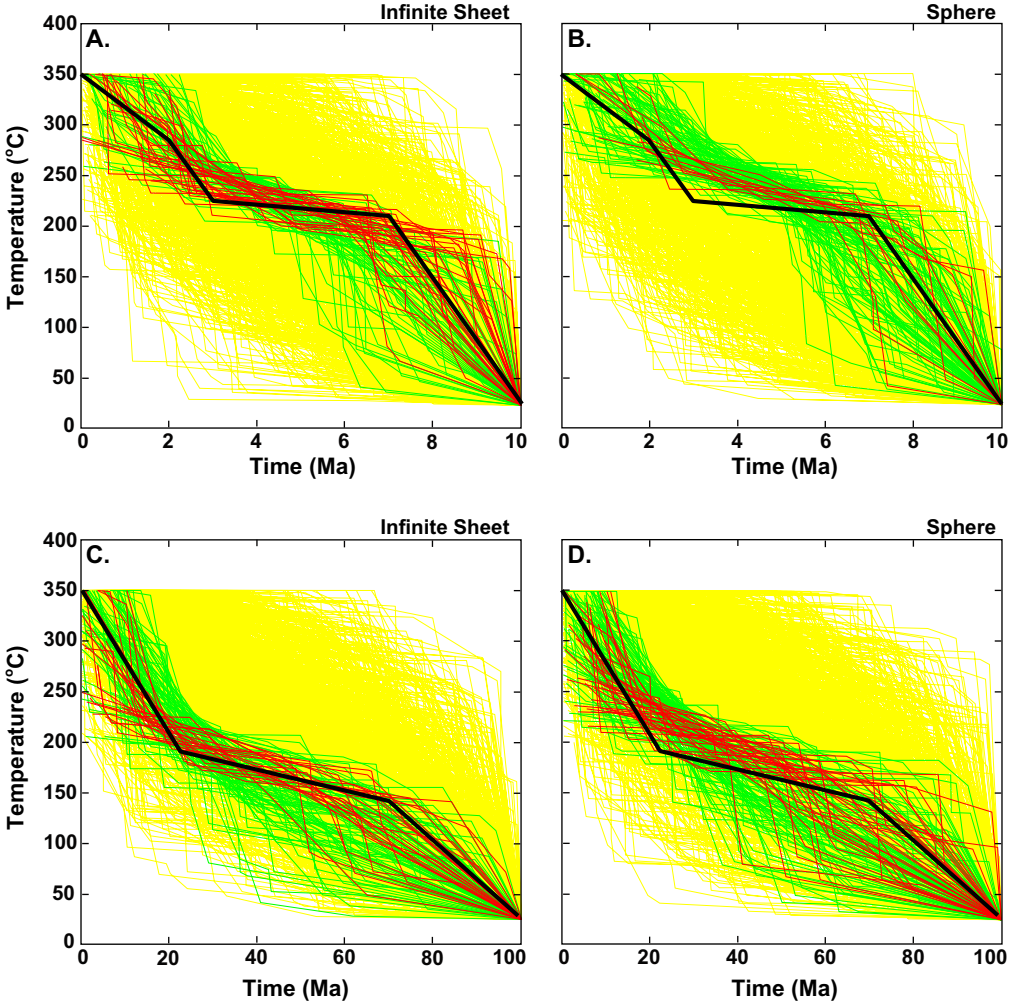

Fig. 12. Summary of monotonic cooling histories that were modeled for both infinite sheet and spherical diffusion geometries using geometry-specific E_a and $\ln(D_o/a^2)$ values calculated from the incremental degassing of the $\varepsilon = \infty$ rectangle (i.e., a infinite sheet; see Table 1). t–T paths that yielded age spectra that best fit the target spectra (see text for details) are shown in red (MSWD < 3). Both infinite sheet and spherical diffusion geometries predict similar cooling histories for a given target age spectrum.

infinite tetragonal prism, we computed F as a function of T and t using our LB code and the Arrhenius relationship in Eq. (13). To compute F as a function of T and t for the infinite sheet and sphere, we used the geometry-specific E_a and $\ln(D_o/a^2)$ values calculated from the incremental degassing of the $\varepsilon = 1$ rectangle (listed in Table 1) and solved the analytical solutions for diffusive loss from an infinite sheet and sphere (see McDougall and Harrison (1999) and references therein). The results are summarized in Fig. 13.

Infinite sheet and spherical diffusion geometries predict significantly different fractional losses for a given t–T pulse, where the infinite sheet is characterized by the larger F. This disparity in F may exceed 0.50 under some t–T conditions, which depend in detail on the contrasting Arrhenius relationships and the duration and temperature of the thermal pulse. By inspection of Fig. 13D and F it is apparent that a sphere more accurately predicts the t–T conditions associated with a given F for the infinite square prism than the infinite sheet does. At a given F and t, infinite sheet and spherical geometries differ by 50 °C or more and provide constraints on the maximum and minimum allowable T, respectively.

7.3. Discussion

The modeling exercises outlined above raise an important question: Why does one's choice of diffusion geometry affect t–T conditions predicted for episodic reheating events, but negligibly influence predicted slow cooling histories? To answer this question we refer to Fig. 7, which depicts the fractional loss (F) as a function of Fourier number ($Fo = Dt/a^2$) for an infinite sheet and a sphere. Depending on the duration and temperature of a given episodic heating event, infinite sheet and spherical geometries may predict similar fractional losses (e.g., circles and squares in Fig. 7) or vastly different fractional losses (e.g., diamonds in Fig. 7). Note that the apparent Fo experienced by the infinite sheet and sphere for a given episodic heating event are not identical because different diffusion parameters are used for the two geometries (see Section 7.2). Thus the error

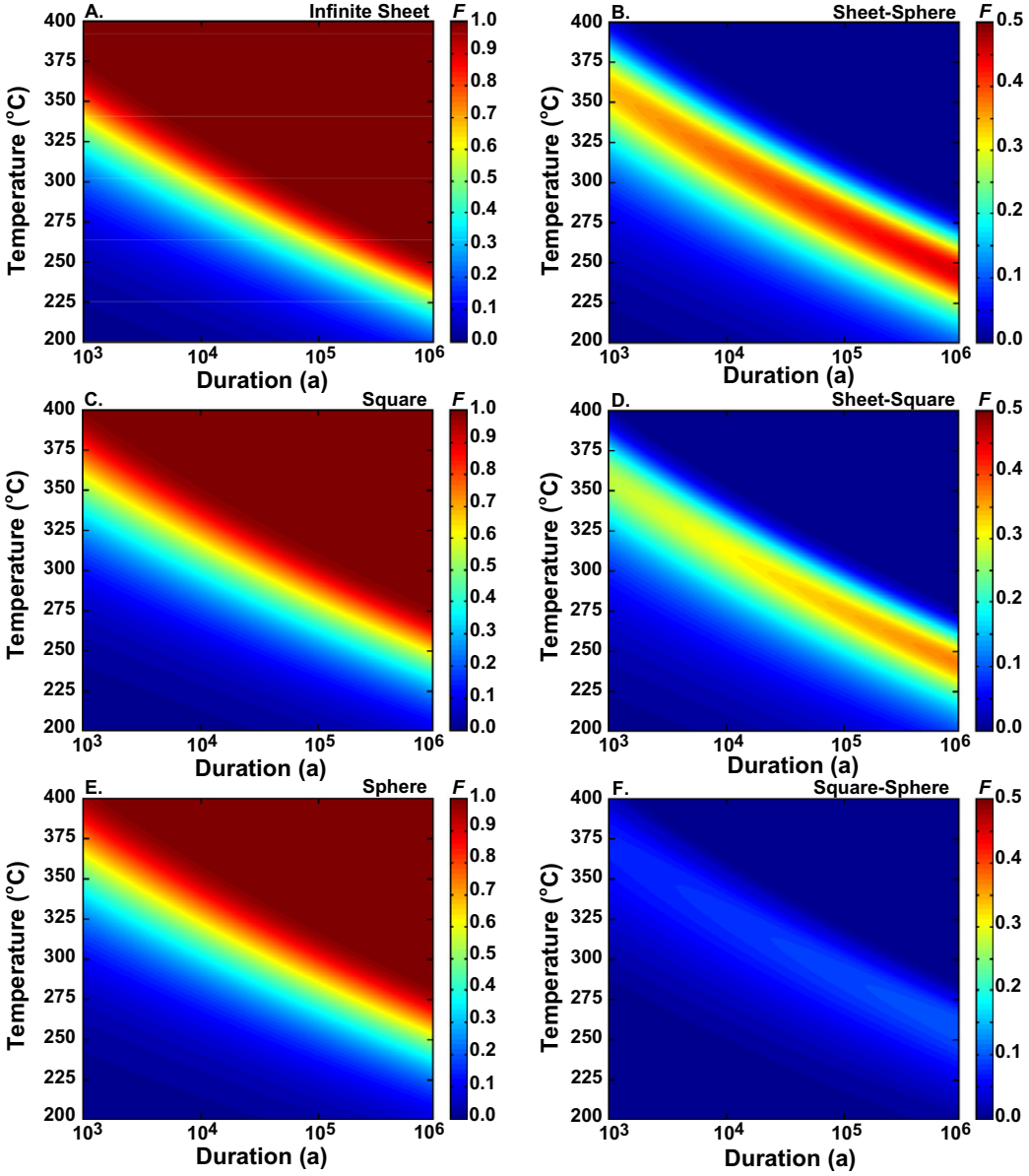

Fig. 13. Comparison of t–T solutions to F calculated for diffusive loss from an $\varepsilon = 1$ rectangle held at a constant temperature (T) for a specified duration (t) (see text for calculation). Results are modeled using (A) the LB diffusion code, (C) infinite sheet geometry, and (E) spherical geometry. For (C) and (E) we used the geometry-specific E_a and $\ln(D_o/a^2)$ values calculated from the incremental degassing of the $\varepsilon = 1$ rectangle (Table 1) and solved the analytical solutions for fractional loss as a function of Fourier number ($Fo = Dt/a^2$). In panels (B), (D), and (F) we compare the differences between these models. A sphere more accurately predicts the t–T conditions associated with a given F for the infinite tetragonal prism ($\varepsilon = 1$ rectangle) than the infinite sheet does.

in t–T conditions associated with a given F depends in detail on the E_a and D_o of the sample and the nature of the heating event.

Unlike some episodic heating events, both infinite sheet and spherical geometries predict similar thermal histories for slowly cooled samples. Consider a hypothetical potassium-bearing sample in which the production of radiogenic ^{40}Ar ($^{40}Ar^*$) is discretized into equally spaced time steps. During cooling, the diffusive loss of each discrete increment of $^{40}Ar^*$ produced can be modeled independently and subsequently summed with the other steps to determine the concentration of the bulk crystal at any time. The fractional loss of a given production step depends on the cumulative Fo (i.e., the thermal history) experienced by that discrete quantity of radiogenic Ar (see small dots in Fig. 7). Early production steps experience larger cumulative Fo whereas later production steps experience smaller cumulative Fo. An observed age spectrum reflects the aggregate of the concentration distributions (i.e., the fractional loss) of each discrete production step. Both geometries predict similar F for many of the production steps and on average the difference in F is much smaller than that associated with some episodic loss events. Furthermore, differences in the morphology of infinite sheet and spherical diffusive loss profiles

(e.g., McDougall and Harrison, 1999) offset differences in the calculated fractional loss (i.e., 20% loss from an infinite sheet yields a similar age spectrum to 16% loss from a sphere). As such, one's choice of diffusion geometry appears to be fairly inconsequential for slow cooling thermal histories (Lovera et al., 1991; Meesters and Dunai, 2002).

8. CONCLUSIONS

(1) We have developed a code based on the lattice Boltzmann (LB) method to model diffusion from a variety of complex 2D and 3D geometries with isotropic, temperature-independent anisotropic, and temperature-dependent anisotropic diffusivity. Our model thereby greatly surpasses the capabilities of widely used analytical solutions requiring simplifying assumptions. We hope in the near future to make a user-friendly version of this code freely available as a software package with an extensive graphical user interface. Further development, documentation, support, and dissemination of the code is envisaged with (pending) funding support. In the interim, interested users can contact us to obtain a copy of the existing codes and additional information can be found at http://huber.eas.gatech.edu/diffusion.html.

(2) Diffusion parameters derived from degassing experiments relating fractional loss to diffusivity using analytical solutions for simple geometries, such as an infinite cylinder, infinite sheet, sphere, or cube, may be subtly but significantly incorrect. Natural crystals with complex topologies should yield modestly curvilinear Arrhenius arrays, where the magnitude of the effect depends on (1) the deviation from an ideal geometry, (2) the fractional release included in the regression, and (3) the heating schedule. A reasonable upper bound on the intrinsic error in calculated E_a that will result from an inappropriate choice of diffusion geometry appears to be ~10%.

(3) Natural crystals that are devoid of microstructure can be relatively accurately modeled as spheres if effective diffusion radii (r_{eff}) are calculated using simple scaling relationships that relate shape and/or diffusive anisotropy to the average normalized distance (AND) for diffusion. The AND approach can be incorporated into analytical and finite-difference production-diffusion codes to obtain accurate thermal histories from geometrically complex crystals having temperature-independent and temperature-dependent anisotropy. Crystals that have complex zoning profiles or microstructural features like fast diffusion pathways, exsolution lamellae, or diffusive sinks require more sophisticated models and cannot be treated as spheres.

(4) One's choice of diffusion geometry in a $^{40}Ar/^{39}Ar$ or $^{4}He/^{3}He$ experiment will negligibly influence a calculated thermal history for samples that have cooled monotonically through the partial retention zone, provided that the same geometry is used to calculate diffusion parameters and forward model potential t–T paths. However, one's choice of diffusion geometry can influence calculated t–T constraints on episodic loss events (e.g., impact events on meteorites and lunar rocks) and burial heating conditions.

ACKNOWLEDGMENTS

The authors acknowledge financial support from the NSF Petrology and Geochemistry program (Grant EAR-0838572 to P.R.R.) and the Ann and Gordon Getty Foundation. W.S. Cassata was supported by a National Science Foundation Graduate Research Fellowship. C. Huber was supported by a Swiss postdoctoral fellowship PBSKP2-128477. Peter Reiners, Cécile Gautheron, and two anonymous reviewers are thanked for their thoughtful and constructive comments.

APPENDIX

An analytical approach to finding AND for a tetragonal prism

The analytical solution for diffusive loss from a tetragonal prism of dimension $2a \times 2b \times 2c$ in the x, y, and z directions, respectively, can be obtained by taking the Fourier transform of the 3D diffusion equation for both time and spatial variables. In the case of a tetragonal prism with a homogeneous initial concentration C_0, we obtain

$$C(x,t) = \frac{64C_0}{\pi^3} \sum_{l,m,n=0}^{\infty} \frac{(-1)^{l+m+n}}{(2l+1)(2m+1)(2n+1)} \times \cos\left(\frac{(2l+1)\pi x}{2a}\right) \cos\left(\frac{(2m+1)\pi y}{2b}\right) \times \cos\left(\frac{(2n+1)\pi z}{2c}\right) \exp\left(-\frac{\pi^2}{4}\frac{D_x(2l+1)^2}{a^2}t\right) \times \exp\left(-\frac{\pi^2}{4}\frac{D_y(2m+1)^2}{b^2}t\right) \exp\left(-\frac{\pi^2}{4}\frac{D_z(2n+1)^2}{c^2}t\right). \quad \text{(A1)}$$

The fractional loss from a tetragonal prism is given by

$$F(t) = 1 - \frac{1}{M_0}\int_0^t \left(\int_V \frac{\partial C(x,t)}{\partial t} dV\right) dt \quad \text{(A2)}$$

where V is the volume of the tetragonal prism ($V = 8abc$) and $M_0 = C_0{}^{*} V$. After some algebra, we obtain

$$F = 1 - \left(\frac{8}{\pi^2}\right)^3 \sum_{l,m,n=0}^{\infty} \frac{1}{(2l+1)^2(2m+1)^2(2n+1)^2} \times \left(\exp(-\frac{\pi^2}{4b^2}D_y(2l+1)^2 t)\right)^{\frac{1}{\varepsilon_1^2}\frac{D_x}{D_y}} \times \exp\left(-\frac{\pi^2}{4b^2}D_y(2m+1)^2 t\right) \times \left(\exp\left(-\frac{\pi^2}{4b^2}D_y(2n+1)^2 t\right)\right)^{\frac{1}{\varepsilon_2^2}\frac{D_z}{D_y}} \quad \text{(A3)}$$

where $\varepsilon_1 = a/b$ and $\varepsilon_2 = c/b$. The infinite sum in Eq. (A3) converges rapidly, and we found that truncating over values of l, m, $n > 5$ is sufficient for obtaining accurate results. We define the exponents on the first and third exponential terms to be Ω_1 and Ω_2, respectively.

The fractional loss out of a body with an arbitrary shape depends on the average effective distance that atoms/molecules must travel to reach the nearest surface/boundary. We use the definition of the normalized distance at every position in the prism $\boldsymbol{x}$, $d(\boldsymbol{x})$

$$d(\mathrm{x}) = \frac{\min\limits_{\mathrm{s}} \left(\frac{\mathrm{x}-\mathrm{x_s}}{\mathscr{D}^{1/2}} \right)}{D_{ref}^{1/2}} \tag{A4}$$

where $\min_S$ is the minimum taken over all the points belonging to the surface S, x and x_S are the coordinates of x V and of the surface S, respectively, and $\mathscr{D}$ is the vector of diffusivities, given by

$$\mathscr{D} = (D_x, D_y, D_z). \tag{A5}$$

We set arbitrarily the reference diffusivity $D_{ref} = D_y$. The average normalized distance is then

$$\mathrm{AND} \equiv \int_V \min_S \left(\frac{\mathrm{x} - \mathrm{x}_S}{(\mathscr{D}/D_y)^{1/2}} \right) dV \tag{A6}$$

We can divide a tetragonal prism shape with dimensions $2a \times 2b \times 2c$ centered at the origin into 8 equal pieces (we will treat the piece in the quadrant $x \geqslant 0$, $y \geqslant 0$ and $z \geqslant 0$, see Fig. A1). The average normalized distance for this quadrant becomes

$$\mathrm{AND} \equiv \frac{8}{V} \int_0^a \int_0^b \int_0^c \min \left(\frac{a-x}{\sqrt{\frac{D_x}{D_y}}}, b-y, \frac{c-z}{\sqrt{\frac{D_z}{D_y}}} \right) dxdydz \tag{A7}$$

To compute this integral, we must divide the volume $0 \leqslant x \leqslant a$, $0 \leqslant y \leqslant b$, $0 \leqslant z \leqslant c$ into three non-overlapping volumes, given by

$$V_x defined\ as\ min \left(\frac{a-x}{\sqrt{\frac{D_x}{D_y}}}, b-y, \frac{c-z}{\sqrt{\frac{D_z}{D_y}}} \right) = \frac{a-x}{\sqrt{\frac{D_x}{D_y}}} \tag{A8}$$

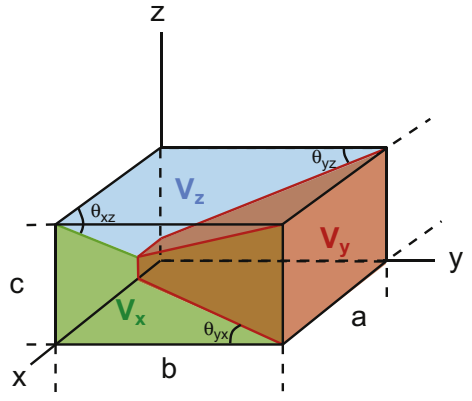

Fig. A1. Schematic depiction the division of a quadrant of a tetragonal prism into V_x, V_y, and V_z. Volume V_x represents the spatial field from which all atoms/molecules will exit the body through the surface with normal along the x-direction.

$$V_y defined\ as\ min \left(\frac{a-x}{\sqrt{\frac{D_x}{D_y}}}, b-y, \frac{c-z}{\sqrt{\frac{D_z}{D_y}}} \right) = b-y \tag{A9}$$

$$V_z defined\ as\ min \left(\frac{a-x}{\sqrt{\frac{D_x}{D_y}}}, b-y, \frac{c-z}{\sqrt{\frac{D_z}{D_y}}} \right) = \frac{c-z}{\sqrt{\frac{D_z}{D_y}}} \tag{A10}$$

Fig. A1 schematically depicts the division of the quadrant into V_x, V_y, and V_z. These volumes are analogous to river drainage basins divided by ridgelines. For example, volume V_x represents the spatial field from which all atoms/molecules will exit the body through the surface with normal along the x-direction. The boundaries between V_x, V_y, and V_z (our ridgelines or drainage divides) depend only on Ω_1 and Ω_2 and are obtained from Eqs. (A8)–(A10). The angle between the boundary of volume V_i and the normal (along the i-direction) in the plane i–j (see Fig. A1) is given by

$$\theta_{ij} = \mathrm{atan}\left(\sqrt{\frac{D_j}{D_i}} \right) \tag{A11}$$

where i and $j = x$, y, and z. Thus six angles describe the volumes. After integrating Eq. (A7) to find the minimum normalized distance to the surface of the object for V_x, V_y, and V_z and summing the three contributions, we obtain

$$\begin{aligned}
\mathrm{AND} = b \Bigg[& -(1-(1-\sqrt{\Omega_1})^4) \frac{\sqrt{\Omega_2}}{4\Omega_1\sqrt{\Omega_1}} \\
& -(1-(1-\sqrt{\Omega_2})^4) \frac{\sqrt{\Omega_1}}{4\Omega_2\sqrt{\Omega_2}} \\
& +(1-(1-\sqrt{\Omega_1})^3) \left(\frac{\sqrt{\Omega_1}}{\Omega_2\sqrt{\Omega_2}} - \frac{1}{3\Omega_2} - \frac{\sqrt{\Omega_1}}{3\Omega_2} \right) \\
& +(1-(1-\sqrt{\Omega_2})^3) \left(\frac{\sqrt{\Omega_2}}{\Omega_1\sqrt{\Omega_1}} - \frac{1}{3\Omega_1} - \frac{\sqrt{\Omega_2}}{3\Omega_1} \right) \\
& +(1-(1-\sqrt{\Omega_1})^2) \left(\frac{1}{\Omega_1} - \frac{\sqrt{\Omega_2}}{\Omega_1} - \frac{3\sqrt{\Omega_2}}{2\Omega_1\sqrt{\Omega_1}} - \frac{1}{2\sqrt{\Omega_1}} \right) \\
& +(1-(1-\sqrt{\Omega_2})^2) \left(\frac{1}{\Omega_2} - \frac{\sqrt{\Omega_1}}{\Omega_2} - \frac{3\sqrt{\Omega_1}}{2\Omega_2\sqrt{\Omega_2}} - \frac{1}{2\sqrt{\Omega_2}} \right) \\
& +\frac{\sqrt{\Omega_1}}{\Omega_2} + \frac{\sqrt{\Omega_2}}{\Omega_1} - \sqrt{\frac{\Omega_1}{\Omega_2}} - \sqrt{\frac{\Omega_2}{\Omega_1}} \\
& -\frac{1}{\sqrt{\Omega_1}} - \frac{1}{\sqrt{\Omega_2}} + \frac{\sqrt{\Omega_1\Omega_2}}{4} - \frac{\sqrt{\Omega_1}}{3} - \frac{\sqrt{\Omega_2}}{3} + \frac{5}{2} \Bigg]
\end{aligned} \tag{A12}$$

The AND value is function of our reference lengthscale b.

Thus the effective radius of an equivalent isotropic sphere is given by

$$r_{eff}(\Omega_1, \Omega_2) = \frac{\mathrm{AND}}{0.2594}. \tag{A13}$$

APPENDIX A. SUPPLEMENTARY DATA

Supplementary data associated with this article can be found, in the online version, at doi:10.1016/j.gca.2011.01.039.

REFERENCES

Bhatnagar P., Gross E. and Krook A. (1954) A model for collisional processes in gases I: small amplitude processes in charged and neutral one component systems. *Phys. Rev.* **94**, 511–525.

Carslaw H. S. and Jaeger J. C. (1959) *Conduction of Heat in Solids*. Oxford University Press, New York.

Cherniak D. J., Watson E. B. and Thomas J. B. (2009) Diffusion of helium in zircon and apatite. *Chem. Geol.* **268**, 155–166.

Chopard B. and Droz M. (1998) *Cellular Automata and Modeling of Physical Systems, Monographs and Texts in Statistical Physics*. Cambridge University Press, Cambridge.

Crank J. (1975) *The Mathematics of Diffusion*. Oxford University Press, New York.

Farley K. A. (2000) Helium diffusion from apatite: general behavior as illustrated by Durango fluorapatite. *J. Geophys. Res.* **105**, 2903–2914.

Farley K. A. (2007) He diffusion systematics inminerals: evidence from syntheticmonazite and zircon structure phosphates. *Geochim. Cosmochim. Acta* **71**, 4015–4024.

Farley K. A. and Reiners P. W. (2001) Influence of crystal size on apatite (U–Th)/He thermochronology: an example from the Bighron Mountains, Wyoming. *Earth Planet. Sci. Lett.* **188**, 413–420.

Fechtig H. and Kalbitzer S. (1966) The diffusion of argon in potassium bearing solids. In *Potassium-Argon Dating* (eds. O. A. Schaeffer and J. Zahringer). Springer, pp. 68–106.

Frisch U., Hasslacher B. and Pomeau Y. (1986) Lattice gas automata for the Navier–Stokes equations, *Phys. Rev. Lett.* **56**, 1505–1508.

Gautheron C. and Tasson-Got L. (2010) A Monte Carlo approach to diffusion applied to noble gas/helium thermochronology. *Chem. Geol.* **273**, 212–224.

Giletti B. J. (1974) Studies in diffusion, I: Ar in phlogopite mica. In *Geochemical Transport and Kinetics* (eds. A. W. Hoffman, B. J. Giletti, H. S. Yoder and R. A. Yund). Carnegie Institute of Washington Publications, pp. 107–115.

Goodwin L. B. and Renne P. R. (1991) Effects of progressive mylonitization on grain size and Ar retention of biotites in the Santa Rosa Mylonite Zone, California, and thermochronologic implications. *Contrib. Mineral. Petrol.* **108**, 283–297.

Hames W. E. and Bowring S. A. (1994) An empirical-evaluation of the argon diffusion geometry in muscovite. *Earth Planet. Sci. Lett.* **124**, 161–167.

Huber C., Parmigiani A., Chopard B., Manga M. and Bachmann O. (2008) Lattice Boltzmann model for melting with natural convection. *Int. J. Heat Fluid Flow* **29**, 1469–1480.

Lovera O. M., Richter F. M. and Harrison T. M. (1991) Diffusion domains determined by ^{39}Ar release during step heating. *J. Geophys. Res.* **96**, 2057–2069.

McDougall I. and Harrison T. M. (1999) *Geochronology and Thermochronology by the $^{40}Ar/^{39}Ar$ Method*. Oxford University Press.

McIntyre G. A., Brooks C., Compston W. and Turek A. (1966) The statistical assessment of Rb/Sr isochrons. *J. Geophys. Res.* **71**, 5459–5468.

Meesters A. G. C. A. and Dunai T. J. (2002) Solving the production–diffusion equation for finite diffusion domains of various shapes. Part I: Implications for low-temperature (U–Th)/He thermochronology. *Chem. Geol.* **186**, 333–344.

Qian Y. H., D'Humi'eres D. and Lallemand P. (1992) Lattice BGK models for the Navier–Stokes equation. *Europhys. Lett.* **17**, 479–484.

Reich M., Ewing R. C., Ehlers T. A. and Becker U. (2007) Low-temperature anisotropic diffusion of helium in zircon: implications for zircon (U–Th)/He thermochronometry. *Geochim. Cosmochim. Acta* **71**, 3119–3130.

Reiners P. (2009) Nonmonotonic thermal histories and contrasting kinetics of multiple thermochronometers. *Geochim. Cosmochim. Acta* **73**, 3612–3629.

Saadoune I. and De Leeuw N. H. (2009) A computer simulation study of the accommodation and diffusion of He in uranium- and plutonium-doped zircon (ZrSiO4). *Geochim. Cosmochim. Acta* **73**, 3880–3893.

Saadoune I., Purton J. A. and De Leeuw N. H. (2009) He incorporation and diffusion pathways in pure and defective zircon $ZrSiO_4$: a density functional theory study. *Chem. Geol.* **258**, 182–196.

Succi S. (2002) *The lattice Boltzmann Equation and Beyond*. Oxford University Press.

Wartho J.-A., Kelley S. P., Brooker R. A., Carroll M. R., Villa I. M. and Lee M. R. (1999) Direct measurement of Ar diffusion profiles in a gem-quality Madagascar K-feldspar using the ultra-violet laser ablation microprobe (UVLAMP). *Earth Planet. Sci. Lett.* **170**, 141–153.

Watson E. B., Wanser K. H. and Farley K. A. (2010) Anisotropic diffusion in a finite cylinder, with geochemical applications. *Geochim. Cosmochim. Acta* **74**, 614–633.

Wolf-Gladrow D. (2000) *Lattice-gas Cellular Automata and Lattice Boltzmann Models: An Introduction*. Springer, p. 308.

Wright N., Layer P. W. and York D. (1991) New insights into thermal history from single grain ^{40}Ar/^{39}Ar analysis of biotite. *Earth Planet. Sci. Lett.* **104**, 70–79.

Associate editor: Peter W. Reiners